Pergamon

Int. J. Multiphase Flow Vol. 24, No. 3, pp. 387–410, 1998
© 1998 Published by Elsevier Science Ltd. All rights reserved
Printed in Great Britain
0301-9322/98 $19.00 + 0.00

PII: S0301-9322(97)00050-5

COMPUTATIONS OF BOILING FLOWS

DAMIR JURIC[1]† and GRÉTAR TRYGGVASON[2]

[1]Theoretical Division, Group T-3, Fluid Dynamics, MS B216, Los Alamos National Laboratory, Los Alamos, NM 87545, U.S.A.
[2]Department of Mechanical Engineering and Applied Mechanics, The University of Michigan, Ann Arbor, MI 48109, U.S.A.

(Received 15 May 1997; in revised form 1 July 1997)

Abstract—A numerical method to simulate liquid–vapor phase change is presented. The method is based on the so-called single field formulation where one set of equations for conservation of mass, momentum and energy are written for the entire flow field. Interfacial source terms for surface tension, interphase mass transfer and latent heat are added as delta functions that are non-zero only at the phase boundary. The equations are discretized by a finite difference method on a regular grid and the phase boundary is explicitly tracked by a moving front. A comparison of numerical results to the exact solution of a one-dimensional test problem shows excellent agreement. The method is applied to film boiling, where vapor bubbles are generated from a thin film next to a hot wall. Although the film boiling simulations presented here are two-dimensional, the resulting heat transfer rate and wall temperatures are found to be in good agreement with experimental observations. © 1998 Published by Elsevier Science Ltd. All rights reserved

Key Words: front tracking, phase change, boiling, film boiling, interface

1. INTRODUCTION

Owing to the ability of fluids to compactly store or liberate large amounts of energy in the form of latent heat upon phase change, boiling and condensation are key processes in the extraction of energy from solar, fossil and nuclear fuels for human use. Among other applications, liquid–vapor phase change is important in the petroleum industry for oil refinement and is currently being investigated by the electronics industry as an effective cooling mechanism for high heat flux electronic devices (Ammerman *et al.* 1996).

Despite its importance and the vast body of research on boiling, the fundamental physical mechanisms involved are far from being understood (Lienhard 1994). Experimental studies have led to the development of numerous empirical correlations specific to particular modes of boiling and surface geometries. However, a more basic understanding is hindered by the small spatial scales and the rapidity of the phase change process both of which make it very difficult to obtain the necessary experimental measurements. Analytical and numerical efforts to understand boiling have focused mainly on simple models of vapor bubble dynamics. An assumed interface shape along with various assumptions concerning surface tension, fluid viscosity and vapor phase velocity and temperature are usually incorporated. Rayleigh (1917) formulated a simplified equation of motion for inertia controlled growth of a spherical vapor bubble. Rayleigh's analysis was extended by, among others, Plesset and Zwick (1954), Prosperetti and Plesset (1978), Mikic *et al.* (1970), Dalle Donne and Ferranti (1975) and Lee (1993) to include thermal and surface tension dominated growth regimes. Lee and Nydahl (1989) and Patil and Prusa (1991) numerically studied hemispherical bubble growth in nucleate boiling.

The complete phase change problem is highly dependent on the simultaneous coupling of many effects none of which can typically be ignored. The modeling of mass, momentum and energy transport must include surface tension, latent heat, interphase mass transfer, discontinuous material properties and complicated liquid–vapor interface dynamics. Phase change with fluid flow is among the more difficult challenges for direct numerical simulations and only

---

†To whom correspondence should be addressed. Tel: (505) 667-2409; Fax: (505) 665-5926; e-mail: djuric@lanl.gov.

recently have numerical methods begun to offer the promise of helping to provide accurate predictions of the detailed small scale physical processes involved. Welch (1995) has made progress in using a two-dimensional, moving mesh, finite volume method to solve the mass, momentum and energy equations for liquid–vapor flows with phase change. However, this method is restricted to flows with only small distortion of the liquid–vapor interface. Son and Dhir (1995) use a moving mesh finite difference method for two-dimensional simulations of phase change. Using grid generation techniques they study the heat transfer and interface behavior in film boiling up to the point of bubble departure.

In this paper we present a two-dimensional front tracking/finite difference method for fluid flow with phase change that enables the simulation of problems with complex motion of the liquid–vapor interface: large interface deformations and topology change. The effects of interphase mass transfer, latent heat, surface tension and unequal material properties between liquid and vapor phases are included. The method is based on a finite difference approximation of the Navier–Stokes and energy equations on an unmoving, structured grid and an explicit tracking of the phase boundary on a moving, unstructured grid. The method is an extension of techniques already developed for isothermal, multifluid flows without phase change in both two and three dimensions by Unverdi and Tryggvason (1992). The multifluid code has been used to investigate the collision of drops (Nobari *et al.* 1996), thermal migration of drops (Nas and Tryggvason 1993) and the motion of clouds of bubbles (Esmaeeli and Tryggvason 1996). The phase change method presented below has also been applied to certain types of combustion problems (Qian *et al.* 1997).

In the following sections of this paper we describe an extensive reformulation of the original isothermal method to allow for fluid flow with phase change. Section 2 is devoted to the mathematical formulation of the phase change problem and Section 3 to the description of the front tracking/finite difference method. In Section 4 we present results from validation tests of the method. Also in Section 4 we focus on the problem of film boiling from an upward facing, heated, flat surface. We present two-dimensional simulations and compare heat transfer results with correlations of experimental data. In Section 5 we discuss some conclusions from this study.

2. MATHEMATICAL FORMULATION

Boiling involves both fluid flow and heat transfer and thus requires the solution of the Navier–Stokes and energy equations. We can write a set of transport equations which is valid in both the liquid and vapor phases. This local, single field formulation incorporates the effect of the interface in the equations as source terms which act only at the interface. These sources account for surface tension and latent heat in the equations for conservation of momentum and energy and for mass transfer across the interface due to phase change in the conservation of mass.

We begin by specifying the material properties which are considered to be constant, but not generally equal for each phase. As a consequence, the bulk fluids are incompressible, but we allow for volume expansion (contraction) at the phase interface due to the density change upon vaporization (condensation). Equations for the material property fields can be written for the entire domain using an indicator function, $I(\mathbf{x},t)$, which has the value 1 in the vapor phase and 0 in the liquid phase. The values of the material property fields at every location are then given by

$$b(\mathbf{x},t) = b_{\mathrm{L}} + (b_{\mathrm{G}} - b_{\mathrm{L}})I(\mathbf{x},t), \qquad [1]$$

where the subscripts G and L refer to the vapor and liquid phases respectively. b stands for density, ρ, specific volume, $\hat{v} = 1/\rho$, viscosity, μ, specific heat, c or thermal conductivity, k.

To find $I(\mathbf{x},t)$ we express it in terms of an integral over a three-dimensional delta function

$$I(\mathbf{x},t) = \int_{\Omega(t)} \delta(\mathbf{x} - \mathbf{x}')\mathrm{d}V'. \qquad [2]$$

The integral is over a volume, $\Omega(t)$, bounded by the phase interface, $\Gamma(t)$. $\delta(\mathbf{x} - \mathbf{x}')$ is a three-dimensional delta function that is non-zero only where $\mathbf{x}' = \mathbf{x}$. $I(\mathbf{x},t)$ is obviously 1 if $\mathbf{x}$ is within $\Gamma(t)$ and 0 otherwise. Taking the gradient of [2] and transforming the volume integral into an integral over the phase interface yields

$$\nabla I = \int_{\Gamma(t)} \mathbf{n}\delta(\mathbf{x} - \mathbf{x}_{\mathrm{s}})\mathrm{d}s, \qquad [3]$$

where $\mathbf{n}$ is the unit normal to the interface, defined to point into the vapor phase and $\mathbf{x}_{\mathrm{s}} = \mathbf{x}(s,t)$ is a parameterization of $\Gamma(t)$. Taking the divergence of [3] results in

$$\nabla^2 I = \nabla \cdot \int_{\Gamma(t)} \mathbf{n}\delta(\mathbf{x} - \mathbf{x}_{\mathrm{s}})\mathrm{d}s. \qquad [4]$$

Thus we find $I(\mathbf{x},t)$ by solving the above Poisson equation where the right-hand-side is a function only of the known interface position at time t. The interface is advected in a Lagrangian fashion by integrating

$$\frac{\mathrm{d}\mathbf{x}_{\mathrm{s}}}{\mathrm{d}t} \cdot \mathbf{n} = V_{\mathrm{n}}, \qquad [5]$$

where $V_{\mathrm{n}} = \mathbf{V} \cdot \mathbf{n}$. $\mathbf{V}$ is the interface velocity vector and V_{n} its normal component. Only the normal component of the interface motion is determined by the physics. The tangential motion is not and we may assume that the interface and fluid at the interface have the same tangential component of velocity (Ishii, 1975).

The conservation of mass equation is also written for the entire flow field

$$\frac{\partial \rho}{\partial t} + \nabla \cdot \mathbf{w} = 0. \qquad [6]$$

Here $\mathbf{w} = \rho\mathbf{u}$ is the fluid mass flux and $\mathbf{u}$ is the fluid velocity field. The time derivative of the density can be rewritten in a more useful form since the density at each point in the domain, [1], depends only on the indicator function which is determined by the known interface location. With the indicator function, $I(\mathbf{x},t)$, to represent the interface, the kinematic equation for a surface moving with velocity, $\mathbf{V}$, is

$$\frac{\partial I}{\partial t} = -\mathbf{V} \cdot \nabla I = -\int_{\Gamma(t)} V_{\mathrm{n}}\delta(\mathbf{x} - \mathbf{x}_{\mathrm{s}})\mathrm{d}s. \qquad [7]$$

Using [7] and [1] for the density, the conservation of mass, [6], can be rewritten as

$$\nabla \cdot \mathbf{w} = \int_{\Gamma(t)} (\rho_{\mathrm{G}} - \rho_{\mathrm{L}})V_{\mathrm{n}}\delta(\mathbf{x} - \mathbf{x}_{\mathrm{s}})\mathrm{d}s. \qquad [8]$$

The momentum equation is written for the entire flow field and the forces due to surface tension are inserted at the interface as body forces which act only at the interface. In conservative form this equation is

$$\frac{\partial \mathbf{w}}{\partial t} + \nabla \cdot (\mathbf{wu}) = -\nabla P + \rho \boldsymbol{g} + \nabla \cdot \boldsymbol{\tau} + \int_{\Gamma(t)} \gamma\kappa\mathbf{n}\delta(\mathbf{x} - \mathbf{x}_{\mathrm{s}})\mathrm{d}s, \qquad [9]$$

where P is the pressure, $\boldsymbol{g}$ is the gravitational force, γ is the surface tension coefficient, κ is twice the mean interface curvature which is positive when the center of curvature lies in the vapor phase and τ is the deviatoric stress tensor for a Newtonian fluid

$$\boldsymbol{\tau} = \mu(\nabla\mathbf{u} + \nabla\mathbf{u}^T). \qquad [10]$$

The integral term in [9] accounts for surface tension acting on the interface. (In order to limit the scope of our study we have assumed that the surface tension coefficient is constant and thus ignored tangential variations in γ along the interface. For a study of Marangoni flows using the front tracking method see Nas and Tryggvason (1993).

The thermal energy equation with an interfacial source term to account for liberation or absorption of latent heat is

$$\frac{\partial}{\partial t}(\rho cT) + \nabla\cdot(\mathbf{w}cT) = -\nabla\cdot\mathbf{q} + \boldsymbol{\tau}{:}\nabla\mathbf{u} - \int_{\Gamma(t)} \dot{m}[L + (c_{\mathrm{L}} - c_{\mathrm{G}})T_{\mathrm{sat}}]\delta(\mathbf{x} - \mathbf{x}_{\mathrm{s}})\mathrm{d}s. \qquad [11]$$

We assume that the constitutive relation for the heat flux, $\mathbf{q} = -k\nabla T$, holds throughout the entire domain. $\boldsymbol{\tau}{:}\nabla\mathbf{u}$ is the viscous dissipation which we include here in the formulation, but neglect in the numerical implementation. T is the temperature and L is the latent heat measured at the equilibrium saturation temperature, $T_{\mathrm{sat}}(P_\infty)$, corresponding to the reference ambient system pressure, P_∞. Unless explicitly written otherwise, T_{sat} will refer to $T_{\mathrm{sat}}(P_\infty)$ throughout the remainder of the paper. $\dot{m}$ is the interfacial mass flux

$$\dot{m} = \rho_{\mathrm{L}}(\mathbf{u}_{\mathrm{L}} - \mathbf{V})\cdot\mathbf{n} = \rho_{\mathrm{G}}(\mathbf{u}_{\mathrm{G}} - \mathbf{V})\cdot\mathbf{n}. \qquad [12]$$

It is important to recognize that away from the interface the single field formulation, [8], [9] and [11], reduces to the customary mass, momentum and thermal energy equations for each of the bulk fluids while at the interface the formulation naturally incorporates the correct mass, momentum and energy balances across the interface. Integration of [8], [9] and [11] across the interface yields [12] above for the mass balance and

$$P_{\mathrm{G}} - P_{\mathrm{L}} = -\dot{m}^2\left(\frac{1}{\rho_{\mathrm{G}}} - \frac{1}{\rho_{\mathrm{L}}}\right) + (\boldsymbol{\tau}_{\mathrm{G}}\cdot\mathbf{n})\cdot\mathbf{n} - (\boldsymbol{\tau}_{\mathrm{L}}\cdot\mathbf{n})\cdot\mathbf{n} + \gamma\kappa, \qquad [13]$$

$$(\boldsymbol{\tau}_{\mathrm{G}}\cdot\mathbf{n})\cdot\mathbf{t} = (\boldsymbol{\tau}_{\mathrm{L}}\cdot\mathbf{n})\cdot\mathbf{t}, \qquad [14]$$

$$(\mathbf{q}_{\mathrm{G}} - \mathbf{q}_{\mathrm{L}})\cdot\mathbf{n} = -\dot{m}[L + (c_{\mathrm{G}} - c_{\mathrm{L}})(T_{\mathrm{s}} - T_{\mathrm{sat}})]$$

$$-\frac{\dot{m}^3}{2}\left(\frac{1}{\rho_{\mathrm{G}}^2} - \frac{1}{\rho_{\mathrm{L}}^2}\right) + \dot{m}\left[\frac{(\boldsymbol{\tau}_{\mathrm{G}}\cdot\mathbf{n})\cdot\mathbf{n}}{\rho_{\mathrm{G}}} - \frac{(\boldsymbol{\tau}_{\mathrm{L}}\cdot\mathbf{n})\cdot\mathbf{n}}{\rho_{\mathrm{L}}}\right] \qquad [15]$$

for the normal momentum, tangential momentum and thermal energy, respectively. (Note that for a static interface, [13] reduces to the well-known Laplace equation, P_{G}–$P_{\mathrm{L}} = \gamma\kappa$.) These jump conditions are identical to those derived by Delhaye (1974) and Ishii (1975) except where we have made the assumptions that the interface is thin and massless, the surface tension coefficient, γ, is constant and the energy contribution due to interface stretching is negligible. In the above equations, $T_{\mathrm{s}} = T(\mathbf{x}_{\mathrm{s}})$ is the interface temperature and $\mathbf{t}$ is the unit tangent to the interface. In deriving [14] and [15] it was postulated that there is no-slip in the tangential fluid velocities across the interface,

$$\mathbf{u}_{\mathrm{G}}\cdot\mathbf{t} = \mathbf{u}_{\mathrm{L}}\cdot\mathbf{t} = \mathbf{V}\cdot\mathbf{t} \qquad [16]$$

and that the temperatures of the vapor and liquid at the interface are equal

$$T_{\mathrm{G}} = T_{\mathrm{L}} = T_{\mathrm{s}}. \qquad [17]$$

2.1. *Interface temperature condition*

To complete our formulation we need to provide an equation for the interface temperature, T_{s}. Customarily, it is assumed that the interface temperature is simply equal to the equilibrium saturation temperature corresponding to the system pressure

$$T_s = T_{sat}(P_\infty). \tag{18}$$

In many cases this is an obvious and adequate assumption for macroscale boiling problems but for the microscale problems of interest here we cannot assume [18] *a priori*. The difficulty in using [18] can be illustrated by observing that when there is a pressure jump, $P_G \neq P_L$, across the interface, as required by [13], then obviously the equilibrium saturation temperatures corresponding to those pressures cannot be equal

$$T_{sat}(P_G) \neq T_{sat}(P_L). \tag{19}$$

This leaves the question of what value to choose for T_s. To deal with this problem, two approaches to modeling the temperature at the interface have been taken in the literature (Huang and Joseph 1992; Huang and Joseph 1993). The first approach assumes [17], but a departure from thermodynamic equilibrium saturation temperatures at the interface, i.e. $T_{sat}(P_G) \neq T_G = T_s = T_L \neq T_{sat}(P_L)$, (Delhaye 1974). The second approach begins with the kinetic theory of gases, assumes that, at the interface, the temperatures are at their thermodynamic equilibrium saturation values, but allows a temperature discontinuity at the interface, i.e. $T_{sat}(P_G) = T_G \neq T_L = T_{sat}(P_L)$, (Schrage 1953).

The correct choice of the temperature boundary condition at a phase interface is still an unresolved issue. However, with some minor assumptions, both approaches lead to the same concept: an interfacial resistance to mass transfer across the interface. Using kinetic theory, Tanasawa (1991) derives an approximate expression for the mass transfer across a simplified liquid–vapor interface

$$T_s - T_{sat} = -\frac{\dot{m}}{\varphi} \tag{20}$$

where the so-called kinetic mobility, φ, describes the relative force of molecular attachment to a surface (the resistance to mass transfer across the interface)

$$\varphi = \frac{2\alpha}{(2-\alpha)} \frac{L}{\sqrt{2\pi R T_{sat}}} \frac{1}{(\hat{v}_G - \hat{v}_L) T_{sat}}. \tag{21}$$

R is the gas constant and α is the evaporation coefficient. α represents the fraction of molecules that depart the interface during vaporization. Its measurement is difficult and values range from 0.04 to 1 depending on the fluid (Tanasawa 1991).

In order to determine a general expression for T_s we begin with the principle of balance of entropy across the interface, i.e. the entropy jump condition, and investigate under what conditions [18] is valid. The balance of entropy across the interface together with [16] and [17] lead to an expression for the jump in the Gibbs function, $g = h - Ts$, (h is the enthalpy and s the entropy) across the interface (Delhaye 1974; Ishii 1975)

$$\dot{m}(g_G - g_L) = -\frac{\dot{m}^3}{2}\left(\frac{1}{\rho_G^2} - \frac{1}{\rho_L^2}\right) + \dot{m}\left[\frac{(\boldsymbol{\tau}_G \cdot \mathbf{n}) \cdot \mathbf{n}}{\rho_G} - \frac{(\boldsymbol{\tau}_L \cdot \mathbf{n}) \cdot \mathbf{n}}{\rho_L}\right] + T_s s', \tag{22}$$

where s' is the irreversible production of entropy at the interface due to the phase change. A natural assumption is that s' is a quadratic function of $\dot{m}$ and the kinetic mobility, φ (Truskinovsky 1993)

$$T_s s' = \frac{\dot{m}^2 L}{\varphi T_{sat}}. \tag{23}$$

Thus the interfacial production of entropy is modeled as a resistance to mass transfer across the interface, an approach commonly used in solidification (Tarshis and Tiller 1966).

[13] and [22] with their right hand sides set equal to zero together with the thermodynamic property relation, $dg = \hat{v}dP - s dT$, lead to the usual equilibrium Clausius–Clapeyron equation for a flat, static interface

$$\frac{dP}{dT} = \frac{s_G - s_L}{\hat{v}_G - \hat{v}_L}, \tag{24}$$

which can be integrated from (T_{sat}, P_∞) to (T_{s},P_{s}) to give an expression for the interface temperature (Alexiades and Solomon 1993)

$$T_{\mathrm{s}} - T_{\mathrm{sat}} = \frac{T_{\mathrm{sat}}}{L}\left(\frac{1}{\rho_{\mathrm{G}}} - \frac{1}{\rho_{\mathrm{L}}}\right)(P_{\mathrm{s}} - P_\infty) - (c_{\mathrm{G}} - c_{\mathrm{L}})\frac{T_{\mathrm{sat}}}{L}\left[T_{\mathrm{s}} \ln \frac{T_{\mathrm{s}}}{T_{\mathrm{sat}}} + T_{\mathrm{sat}} - T_{\mathrm{s}}\right]. \qquad [25]$$

P_∞ and P_{s} are the reference ambient system pressure and the pressure at the interface, respectively.

In general the interface is neither flat, nor is its motion reversible. Thus considering [13] and [22] with right-hand-sides included leads, by an analogous procedure, to a more complex, but more complete, expression for the interface temperature

$$T_s - T_{\mathrm{sat}} = \overset{A}{\boxed{\frac{T_{\mathrm{sat}}}{L}\left(\frac{1}{\rho_G} - \frac{1}{\rho_L}\right)(P_s - P_\infty)}} - \overset{B}{\boxed{\frac{(c_G - c_L)}{L}(T_s - T_{\mathrm{sat}})^2}}$$
$$+ \overset{C}{\boxed{\frac{\gamma T_{\mathrm{sat}}\kappa}{2L}\left(\frac{1}{\rho_L} + \frac{1}{\rho_G}\right)}} - \overset{D}{\boxed{\frac{1}{2}\frac{T_{\mathrm{sat}}}{L}\left(\frac{1}{\rho_G} - \frac{1}{\rho_L}\right)[((\boldsymbol{\tau}_G + \boldsymbol{\tau}_L)\cdot \mathbf{n})\cdot \mathbf{n}]}} - \overset{E}{\boxed{\frac{\dot{m}}{\varphi}}}, \qquad [26]$$

where we have linearized the logarithm term and made the assumption that the interface pressure is the average of the pressures in the liquid and vapor at the interface, $P_{\mathrm{s}} = (P_{\mathrm{G}} + P_{\mathrm{L}})/2$. Using arguments from irreversible thermodynamics together with kinetic theory Bornhorst and Hatsopoulos (1967a,b) derived a similar equation for the case of spherical bubble growth.

Clearly the above equation reduces to [18] if all of the boxed terms on the right side are neglected and to [20] if terms A–D can be neglected. In order to investigate the importance of these terms relative to T_{sat} we have performed a simple scale analysis for several different fluids.

If we consider a typical situation in saturated pool film boiling where the imposed wall heat flux, q_{w}, is equal to the heat flux in the vapor, $\mathbf{q}_{\mathrm{G}}\cdot\mathbf{n}$, and the heat flux in the liquid, $q_{\mathrm{L}}\cdot\mathbf{n}$, is small, then [15] (ignoring the last two terms and the difference in specific heats) gives a reasonable average estimate of $\dot{m}$ over the entire interface

$$\dot{m} = -\frac{q_{\mathrm{w}}}{L}. \qquad [27]$$

Experimental boiling curves for various fluids indicate that q_{w}/L ranges from about 0.1 at the minimum film boiling point to above 3 for very high heat flux film boiling.

We introduce suitable scales of length, $\lambda_{\mathrm{d}} = 2\pi(3\gamma/G(\rho_{\mathrm{L}} - \rho_{\mathrm{G}}))^{1/2}$, velocity, $(G\lambda_{\mathrm{d}})^{1/2}$, and pressure (measured from P_∞), $\rho_{\mathrm{L}} G\lambda_{\mathrm{d}}$, where G is Earth gravity and λ_{d} is the most unstable wavelength of the inviscid Rayleigh–Taylor instability. Taking as examples the properties of hydrogen, water, nitrogen and R-113 (Maddox 1983), table 1 indicates the magnitudes, as a percentage of T_{sat}, of the five boxed terms on the right side of [26], labeled A–E, consecutively.

Table 1. Relative magnitudes of the boxed terms on the right side of [26] as a percentage of T_{sat}. Values are given in per cent. Thermal properties are from Maddox (1983)

		Term in [26]				
Fluid	P_∞ (atm)	*A*	*B*	*C*	*D*	*E*
H_2	8	0.13	0.001	0.065	5.1×10^{-6}	0.35
H_2	1	2.1	0.021	0.9	4.8×10^{-5}	1.90
H_2O	1	19.0	3.68	8.0	3.9×10^{-4}	1.22
N_2	1	10.0	0.92	4.2	5.2×10^{-4}	0.65
R-113	1	17.0	6.76	7.2	1.3×10^{-3}	0.44

For, C, the surface tension term, we anticipate maximum curvatures in our calculations on the order of $100/\lambda_d$. For the calculation of the entropy production term, E, we used [21] for φ, with $\alpha = 1$ and [27] for $\dot{m}$, with $q_w/L = 1$. We note that the values in column E represent an average $\dot{m}$ over the entire interface. In reality, most of the vaporization takes place along select portions of the interface that lie close to the heated wall. These regions can have values of $\dot{m}$ one or two orders of magnitude higher than the average. For the specific heat term, B, we estimated T_s–T_{sat} iteratively.

We conclude that we can safely neglect the term due to viscous stress, D, in [26]. Tests of our code on film boiling of hydrogen, described later in Section 4, indicate that terms A, B and C are relatively small for hydrogen and neglecting them only slightly alters the results. We also find that term E can be neglected, but only up to the point where the interface comes close to the heated wall. In general we retain terms A, B, C and E and thus the interface temperature condition that we use is

$$T_s - T_{sat} - \frac{T_{sat}}{L}\left(\frac{1}{\rho_G} - \frac{1}{\rho_L}\right)(P_s - P_\infty) + \frac{(c_G - c_L)}{L}(T_s - T_{sat})^2$$

$$-\frac{\gamma T_{sat}\kappa}{2L}\left(\frac{1}{\rho_L} + \frac{1}{\rho_G}\right) + \frac{\dot{m}}{\varphi} = 0. \qquad [28]$$

In two-dimensions the set of [1], [4], [5], [8], [9] and [11] along with the interface temperature condition, [28], are 11 equations in 11 unknowns. The numerical method for their solution is described in the following section.

3. NUMERICAL METHOD

The numerical technique combines ideas from the front tracking methods developed originally for isothermal multifluid flows (Unverdi and Tryggvason 1992) and solidification without fluid flow (Juric and Tryggvason 1996). The addition of phase change and heat transfer to the fluid dynamics problem has required extensive reformulation of the original isothermal method. In this section we place emphasis on describing the new concepts and essential features of the method as it is applied to boiling flows and specifically to the numerical solution of the set of equations given above.

3.1. *Front tracking*

The interface is represented by separate, non-stationary computational points connected to form a one-dimensional front which lies within the two-dimensional stationary mesh. The interface points are used to calculate geometric information. We find the curvature, normal and tangent at each interface point by fitting a fourth-order polynomial through each point and two adjacent points on either side of that point. The front is advected normal to itself in a Lagrangian fashion by the discrete form of [5]

$$\left(\mathbf{x}_s^{n+1} - \mathbf{x}_s^n\right) \cdot \mathbf{n}^{n+1} = \Delta t V_n, \qquad [29]$$

where superscript n denotes the time level. The motion of the front is in turn used to advect the discontinuous material property fields, [1], by solving the Poisson equation, [4], for the indicator function, $I(\mathbf{x},t)$, at $\mathbf{x}_s^{n+1}$.

The interface deforms greatly in our simulations and it is necessary to add and delete interface points during the course of the calculation such that the distance between adjacent points, r, is maintained on the order of the stationary grid spacing. For our simulations we have used $0.4 < 2r/(h_x + h_y) < 1.6$ where h_x and h_y are, respectively, the horizontal and vertical grid cell dimensions. To accommodate topology changes, interfaces are allowed to reconnect when either parts of the same interface or parts of two separate interfaces come close together. The instantaneous change in topology is, of course, only an approximation of what happens in reality. Since it is not well known at what distance the interfaces will coalesce when brought together and we cannot resolve distances down to such a small scale, we artificially reconnect the interface when two points come closer than a small distance, usually on the order of a grid cell size. This distance is chosen rather arbitrarily for lack of a better physical model, but here the advantage of front tracking is evident since we can control and vary the distance at which interfaces merge and study the effect on topology changes. While the above modifications to the interface are a major task for fully three-dimensional simulations, here the interface is simply a line and they are relatively straightforward. The interface points are connected by forward and backward linked lists and interface restructuring is simply a matter of resetting pointers.

At each time-step, information must be passed between the moving Lagrangian interface and the stationary Eulerian grid since the Lagrangian interface points, $\mathbf{x}_p$, do not necessarily coincide with the Eulerian grid points, $\mathbf{x}_{ij}$. This is done by a method that has become known as the Immersed Boundary Technique which was introduced by Peskin (1977) for the analysis of blood flow in the heart. With this technique, the infinitely thin interface is approximated by a smooth distribution function that is used to distribute the sources at the interface over grid points nearest the interface. In a similar manner, this function is used to interpolate field variables from the stationary grid to the interface. In this way, the front is given a finite thickness on the order of the mesh size to provide stability and smoothness. There is also no numerical diffusion since this thickness remains constant for all time.

Writing the integrals in [4], [8], [9] and [11] in a general form

$$\Phi = \int_{\Gamma(t)} \phi \delta(\mathbf{x} - \mathbf{x}_s) \mathrm{d}s, \tag{30}$$

the discrete interface sources, ϕ_p, can be distributed to the grid and the discrete field variables, R_{ij} (representing $\mathbf{w}$, P or T), can be interpolated to the interface by the discretized summations

$$\Phi_{ij} = \sum_p \phi_p D_{ij}(\mathbf{x}_p) \Delta l_p, \tag{31}$$

$$R_p = \sum_{ij} h_x h_y R_{ij} D_{ij}(\mathbf{x}_p), \tag{32}$$

where Δl_p is the average of the straight line distances from the point p to the two points on either side of p.

[31] is the discretized form of [30] where we have approximated the Dirac function by the distribution function, D_{ij}. For $\mathbf{x}_p = (x_p, y_p)$ we use the distribution function suggested by Peskin and McQueen (1994)

$$D_{ij}(\mathbf{x}_p) = \frac{\mathrm{d}(x_p/h_x - i)\mathrm{d}(y_p/h_y - j)}{h_x h_y}, \tag{33}$$

where

$$\mathrm{d}(r) = \begin{cases} \mathrm{d}_1(r), & |r| \leq 1, \\ 1/2 - \mathrm{d}_1(2 - |r|), & 1 < |r| < 2, \\ 0, & |r| \geq 2, \end{cases}$$

and

$$\mathrm{d}_1(r) = \frac{3 - 2|r| + \sqrt{1 + 4|r| - 4r^2}}{8}.$$

3.2. *Finite difference method*

Once the source terms in [4], [8], [9] and [11] have been distributed to the grid these equations are then discretized and solved using the following finite difference techniques.

To calculate the material property fields, [1], we first find the indicator function using a fast Poisson solver to solve [4]

$$\nabla_h^2 I^{n+1} = \nabla_h \cdot \mathbf{G}^{n+1}. \qquad [34]$$

The subscript h denotes a finite difference approximation to the operator. Here $\mathbf{G}$ is the approximation to the surface integral in [4] calculated using [31]. The indicator function calculated in this way is constant within each material region, but has a finite thickness transition zone around the interface. In this transition zone the indicator function and thus the material properties change smoothly from the value on one side of the interface to the value on the other side. The thickness of the transition zone is only a function of the mesh size and is constant during the calculation. No numerical diffusion is introduced. Another advantage of this approach is that close interfaces can interact in a natural way since contributions to $\mathbf{G}$ calculated from the grid distribution, [31], simply cancel.

Next we calculate the fluid variables $\mathbf{u}$, P and T by means of a phase change projection method. Using a first order, forward Euler time integration the discrete form of [8] and [9] can be written as

$$\nabla_h \cdot \mathbf{w}^{n+1} = M^{n+1}, \qquad [35]$$

$$\frac{\mathbf{w}^{n+1} - \mathbf{w}^n}{\Delta t} = \mathbf{A}^n + \mathbf{F}^{n+1} - \nabla_h P, \qquad [36]$$

where the advection, diffusion and gravitational terms in [9] are lumped into $\mathbf{A}$ and the surface integrals in [8] and [9] are denoted by M and $\mathbf{F}$, respectively.

Following the spirit of the projection algorithm of Chorin (1968), we split the momentum equation into

$$\frac{\tilde{\mathbf{w}} - \mathbf{w}^n}{\Delta t} = \mathbf{A}^n + \mathbf{F}^{n+1} \qquad [37]$$

and

$$\frac{\mathbf{w}^{n+1} - \tilde{\mathrm{w}}}{\Delta t} = -\nabla_h P, \qquad [38]$$

where we introduce the variable $\tilde{\mathbf{w}}$ which is the new fluid mass flux if the effect of pressure is ignored. The first step is to find this mass flux using [37]

$$\tilde{\mathbf{w}} = \mathbf{w}^n + \Delta t(\mathbf{A}^n + \mathbf{F}^{n+1}). \qquad [39]$$

Then the pressure is found by taking the divergence of [38] and using [35]. This leads to a Poisson equation for the pressure

$$\nabla_h^2 P = \frac{\nabla_h \cdot \tilde{\mathbf{w}} - M^{n+1}}{\Delta t}, \qquad [40]$$

which can be solved using a standard fast Poisson solver. The updated mass flux is then found from [38]

$$\mathbf{w}^{n+1} = \tilde{\mathbf{w}} - \Delta t \nabla P. \qquad [41]$$

The updated velocity is simply $\mathbf{u}^{n+1} = \mathbf{w}^{n+1}/\rho^{n>+1}$.

Once the velocity is known, the discretized energy equation, [11], is solved for the temperature field

$$T^{n+1} = \frac{\rho^n c^n T^n + \Delta t(B^n + Q^{n+1})}{\rho^{n+1} c^{n+1}}, \qquad [42]$$

where the advection and diffusion terms in [11] are lumped into B and the surface integral in [11] is denoted by Q.

Note that the time integration is explicit but the source terms, **G**, M, **F** and Q, are evaluated in [31] implicitly at the new time $n + 1$. An important advantage of this is that stability constraints on the time step due to propagation of capillary waves are removed by the implicit treatment of surface tension, **F**.

For the spatial discretization we use the staggered mesh, MAC method of Harlow and Welch (1965). The pressure, temperature, and indicator function are located at the cell centers, the x-component of velocity at vertical cell faces and the y-component of velocity at horizontal cell faces. The spatial derivatives are approximated by second-order centered differences.

The calculation of the stresses in **A** requires special treatment due to the finite numerical thickness of the transition zone across the interface. Due to the phase change, the divergence of the velocity field is non-zero in a finite zone around the interface, and this results in an artificial normal viscous stress that can cause local pressure spikes. To avoid this difficulty we subtract the stresses due to this non-zero divergence from the viscous stresses. Thus **A** is

$$\mathbf{A} = -\nabla_h \cdot (\mathbf{wu}) + \rho\mathbf{g} + \nabla_h \cdot \mu[\nabla_h\mathbf{u} + \nabla_h\mathbf{u}^T - 2(\nabla_h \cdot \mathbf{u})|\mathbf{I}], \tag{43}$$

where **I** is the identity tensor. Note that if viscous dissipation had been included in the energy equation a similar correction would have been necessary for that term.

3.3. *Iterative solution procedure*

Given an initial interface shape the indicator function and material property fields are calculated from [34] and [1]. With appropriate initial conditions for the velocity, and temperature the solution algorithm proceeds iteratively through the following steps:

1. B^n is calculated for [42]. $\mathbf{A}^n$ is calculated for [36] using [43].
2. Using an estimate of the normal interface velocity, V_n, the interface is advected to a new position by [29].
3. At this new interface position, the source terms $\mathbf{G}^{n+1}$, M^{n+1}, $\mathbf{F}^{n+1}$ and Q^{n+1} are calculated using [31].
4. The density, ρ^{n+1}, and specific heat, c^{n+1} at the new interface position are found from the solution to [34] and [1].
5. With appropriate wall boundary conditions and $\mathbf{A}^n$ and B^n calculated in step 1, [35], [36] and [42] are solved for the velocity, pressure and temperature at time $n + 1$ using the phase change projection method described above.
6. The interface temperature condition, [28], is calculated: The temperature, pressure and fluid mass flux at time $n + 1$ are interpolated by [32] to find the temperature, T_s, pressure, P_s, and interfacial mass flux, $\dot{m}$, at each point on the interface found in step 2.
7. If the interface temperature condition is satisfied then the viscosity and thermal conductivity fields are updated to the new interface position found in step 2 by [34] and [1] and the computation proceeds to the next time step. Otherwise, a new estimate for the updated normal velocity, V_n, is found at each interface point using [44] below and the procedure returns to step 2.

In the last step, the new estimate for V_n can be found by an iterative method. In general, if the interface temperature, pressure and interfacial mass flux found in step 6 are substituted into [28] the right hand side of this equation will not equal zero, but some residual error, $E(V_n)$. In order to make this error converge to zero and thus satisfy [28] the iteration method described below is used.

3.4. *Modified Newton iteration*

In matrix form, the Newton iteration updates the unknown velocities at each point by the equation,

$$\mathbf{V}_n^{l+1} = \mathbf{V}_n^l - [\mathbf{J}]^{-1}\mathbf{E}^l(\mathbf{V}_n^l), \tag{44}$$

where l is the iteration index. $\mathbf{V}_n$ and **E** are, respectively, the $N \times 1$ column vectors of normal interface velocities and errors at each point. N is the number of interface points. The Jacobian,

J, is the $N \times N$ matrix of partial derivatives of the error with respect to the velocities. Since these derivatives are difficult to calculate and the subsequent matrix inversion would be computationally expensive, a different Jacobian is used which has the simple form,

$$\mathbf{J} = a^{-1}\mathbf{I}, \qquad [45]$$

where **I** is the identity matrix and a is a constant. This constant determines the rate of convergence of the iteration. At the optimum value of a, which is different for different physical parameters, the iteration converges rather quickly to a tolerance of $\epsilon = 10^{-5}$ in 3 to 10 iterations. The tolerance is calculated by

$$\epsilon = \max\left(\epsilon, \left|V_{n_p}^{l+1} - V_{n_p}^{l}\right|\right), p = 1, N. \qquad [46]$$

Optimum values for a were determined through experimentation with the code and range roughly between 1 and 10.

4. RESULTS AND DISCUSSION

4.1. *Comparison with an exact solution*

We tested the numerical method by comparing numerical results with the exact solution of a simple one-dimensional problem. The one-dimensional problem consists of a heat flux, q_w, applied to the bottom of a rigid wall at $y = 0$. The domain contains a liquid $0 \leq y \leq 0.5$ below its vapor $0.5 \leq y \leq 1$. The top of the domain at $y = 1$ remains open to allow for the vapor to exit due to fluid expansion at the interface. The density ratio is set to $\rho_L/\rho_G = 2$. All other material properties are equal. To make the problem dimensionless we scale lengths by a reference length, l, velocities by a reference velocity, U_o, the heat flux by $\rho_L L$ and the pressure (measured from the reference ambient system pressure, P_∞) by $\rho_L U_0^2$. For this calculation $q_w = 0.05$ and there is no gravity.

For slow interface motion the heat flux in the liquid remains approximately constant and the interface moves downward at a steady velocity. Then exact steady-state solutions for the interface velocity, y-component of fluid velocity and pressure are

$$V = -q_w, v_L = 0, v_G = \left(1 - \frac{\rho_L}{\rho_G}\right)V, \quad P = \left(\frac{\rho_L}{\rho_G} - 1\right)V^2. \qquad [47]$$

After a short initial transient, the calculated interface velocity smoothly asymptotes to the correct steady state value of the exact solution, $V = -0.05$.

Results for the vertical fluid velocity, figure 1(a), and pressure, figure 1(b), are shown at $t = 1.4$ for three grid resolutions, 10×10, 20×20 and 40×40. Even at crude resolutions the numerical results in the bulk liquid and vapor are in excellent agreement with the exact solution. At the interface the exact solution is perfectly discontinuous while the numerical interface has a finite thickness which decreases as the resolution increases. This behavior demonstrates the convergence with increasing grid resolution of the front tracking approach to modeling discontinuities across an interface. The front tracking method inherently distributes the effects of the interface smoothly to mesh points in a localized region near the interface. Thus as the resolution increases these effects become sharper and more localized near the interface. Higher density ratios, up to $\rho_L/\rho_G = 1000$, were also tested and the results were equally as good.

4.2. *Film boiling*

We now turn to a more challenging test of the numerical method, the solution of a two-dimensional film boiling problem. In film boiling, a layer of vapor is located below a layer of liquid and completely blankets a heated surface. Gravity results in the onset of a Rayleigh–Taylor instability of the liquid–vapor interface. The liquid falls toward the wall as the vapor rises. Evaporation of the liquid as it approaches the hot wall prevents the liquid from contacting the wall and provides vapor to the rising bubbles. A balance is maintained between vapor gener-

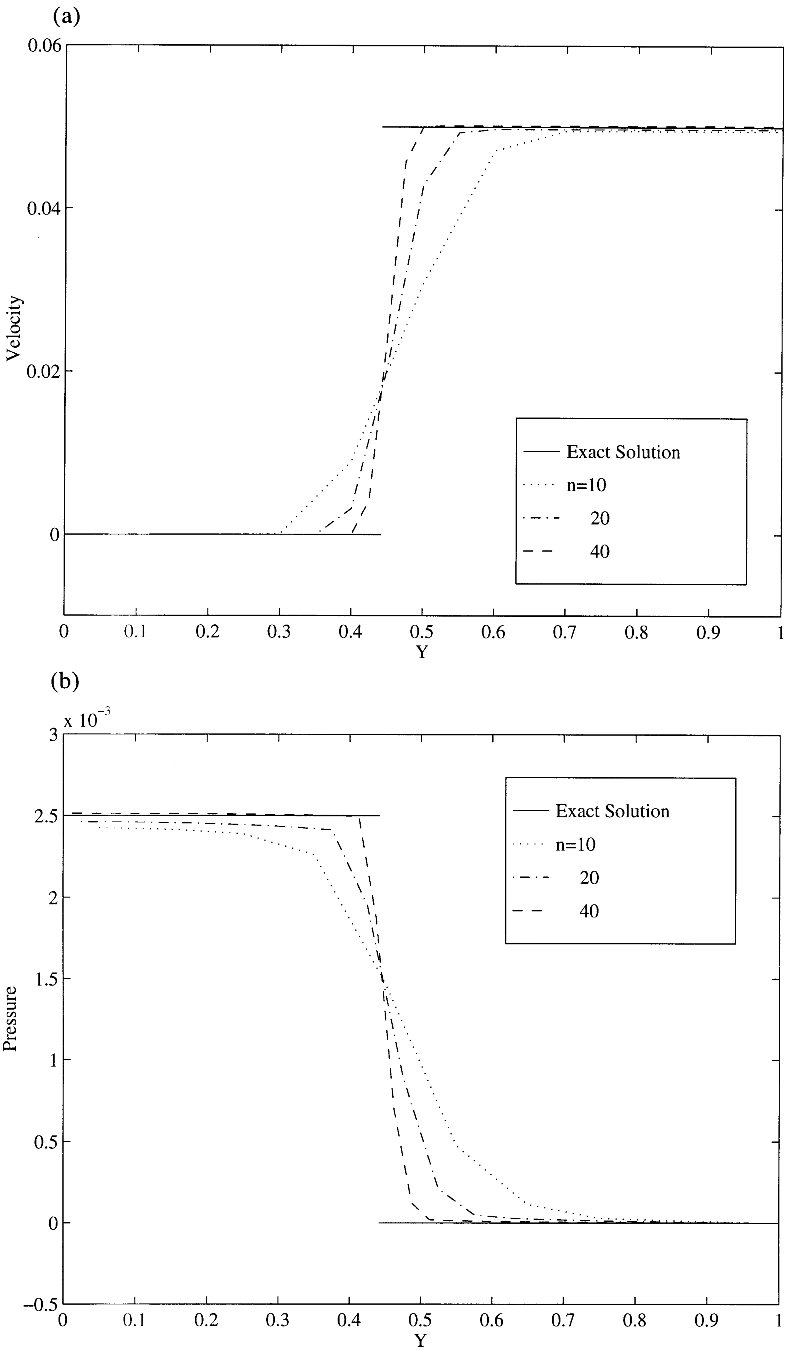

Figure 1. A one-dimensional evaporation test problem. A heat flux, $q_w = 0.05$ is applied to the wall at $y = 0$. The domain contains a liquid $0 \leq y \leq 0.5$ below its vapor $0.5 \leq y \leq 1$. After a short time the liquid evaporates and the liquid–vapor interface moves steadily downward. The density ratio is set to $\rho_L/\rho_G = 2$. All other material properties are equal. The numerical results for (a) the y-component of fluid velocity and (b) the pressure at three different grid resolutions are compared to the exact solution. Even at crude resolutions the numerical results in the bulk liquid and vapor are in excellent agreement with the exact solution. At the interface the exact solution is perfectly discontinuous while the numerical interface has a finite thickness which decreases as the resolution increases.

ation due to vaporization at the liquid–vapor interface and vapor removal due to the break off and rise of vapor bubbles from the interface.

By defining scales of length, $l = \left(\mu_L^2/G\rho_L^2\right)^{1/3}$, velocity, $U_o = (Gl)^{1/2}$, gravity, G, temperature (measured from T_{sat}), $\rho_G L/\rho_L c_L$ and pressure (measured from the reference ambient system pressure, P_∞), $\rho_L Gl$, the problem can be characterized by the Morton number, $M = \mu_L^4 G/\gamma^3 \rho_L$, the Prandtl number, $Pr = \mu_L c_L/k_L$, a capillary parameter, $\sigma = c_L T_{sat}\gamma/\rho_G L^2 l$ and the nondimensional kinetic mobility, $\vartheta = \rho_L^2 c_L U_0/\rho_G L\varphi$. In addition, the Nusselt number, $Nu = k_L q_w/k_G T_w$, is formed using the nondimensional wall heat flux, q_w, (the dimensional wall heat flux scaled by $\rho_G k_L L/\rho_L c_L l$) and wall temperature, T_w. Note that the Nusselt number is not set beforehand, but can change both spatially and temporally during the calculation depending on the value of the local wall temperature, T_w.

The computations are performed in a rectangular domain which is periodic in the x-direction. To allow for vaporization, fluid is allowed to exit at the top boundary where the pressure is specified to be zero. The temperature field is initially zero everywhere with a heat flux, q_w, applied to the rigid bottom wall.

Figure 2 shows results of a film boiling calculation at four different times, t = 2, 14, 30, 40. The calculation is performed in a computational box of dimensions (H_x, H_y) = (57.4, 180), with 150×300 grid resolution and the following dimensionless parameters:

$$\frac{\rho_L}{\rho_G} = 5.22, \frac{\mu_L}{\mu_G} = 3.37, \frac{k_L}{k_G} = 3.42, \frac{c_L}{c_G} = 0.882,$$

$$q_w = 10, Pr = 1.51, M = 10^{-3}, \sigma = 0.024, \vartheta = 0.03.$$

Except for the Morton number, these parameters correspond to those of hydrogen at 8 atm pressure (Maddox 1983). The actual Morton number for hydrogen is about 7.5×10^{-12}. The interface is given an initial shape described by

$$y_s = y_c + \epsilon_s[\cos(2\pi n_s x_s/H_x) + \sin(\pi n_s x_s/H_x)] \qquad [48]$$

where y_c, ϵ_s and n_s are the average initial interface height, perturbation amplitude and perturbation mode, respectively. For this run we choose a two-mode shape: $y_c = 12$, $\epsilon_s = -4$, $n_s = 2$. The horizontal dimension of the box, $H_x = 57.4$, is 1.5 times the most unstable wavelength of the inviscid Rayleigh–Taylor instability, $\lambda_d^* = 2\pi\left[3/\left(M^{1/3}(1-\rho_G/\rho_L)\right)\right]^{1/2}$.

In each frame, the interface is plotted as the solid black line. The left half shows the temperature field as shades of gray with black being the hottest and white the coolest. The temperature scale is the same for all four frames. (To better illustrate the temperature field in this plot, temperatures above 60 are shown as black. The temperatures for this calculation actually range from 0 to 210 with the highest temperatures being at the wall.) The right half shows velocity vectors which, for clarity, are plotted only at every eighth grid point. In figure 2 the liquid–vapor interface begins to exhibit a Rayleigh–Taylor instability with the formation of counter-rotating vortices. The larger of the two bulges grows quickly (b), is released from the vapor layer and forms a rising vapor bubble (c). The smaller bulge is pushed down as cold liquid is forced toward the bottom wall by the upward motion of the adjacent bubble. More vapor is generated since the liquid rapidly evaporates as it approaches the wall. Contact of the liquid with the wall is thus prevented. (At a lower wall heat flux, wall contact should occur, but the study of this effect and nucleate and transition boiling regimes is the subject of future work.) In (d) the upward motion of the bubble causes this additional vapor to be pulled away from the wall to form a second bubble directly underneath the first.

This so-called parent–son bubble behavior has been observed in experiments by Shoji *et al.* (1990). Studying film boiling from a copper sphere, they noticed that, at high heat flux when vapor is rapidly being produced, a son bubble forms just as the parent is released. The son is entrained and elongated by the recirculatory flow behind the parent and is pulled from the surface more quickly. The effective diameter of both bubbles was roughly the same. The simulation here shows precisely these qualitative features of the parent–son bubble behavior: recirculatory

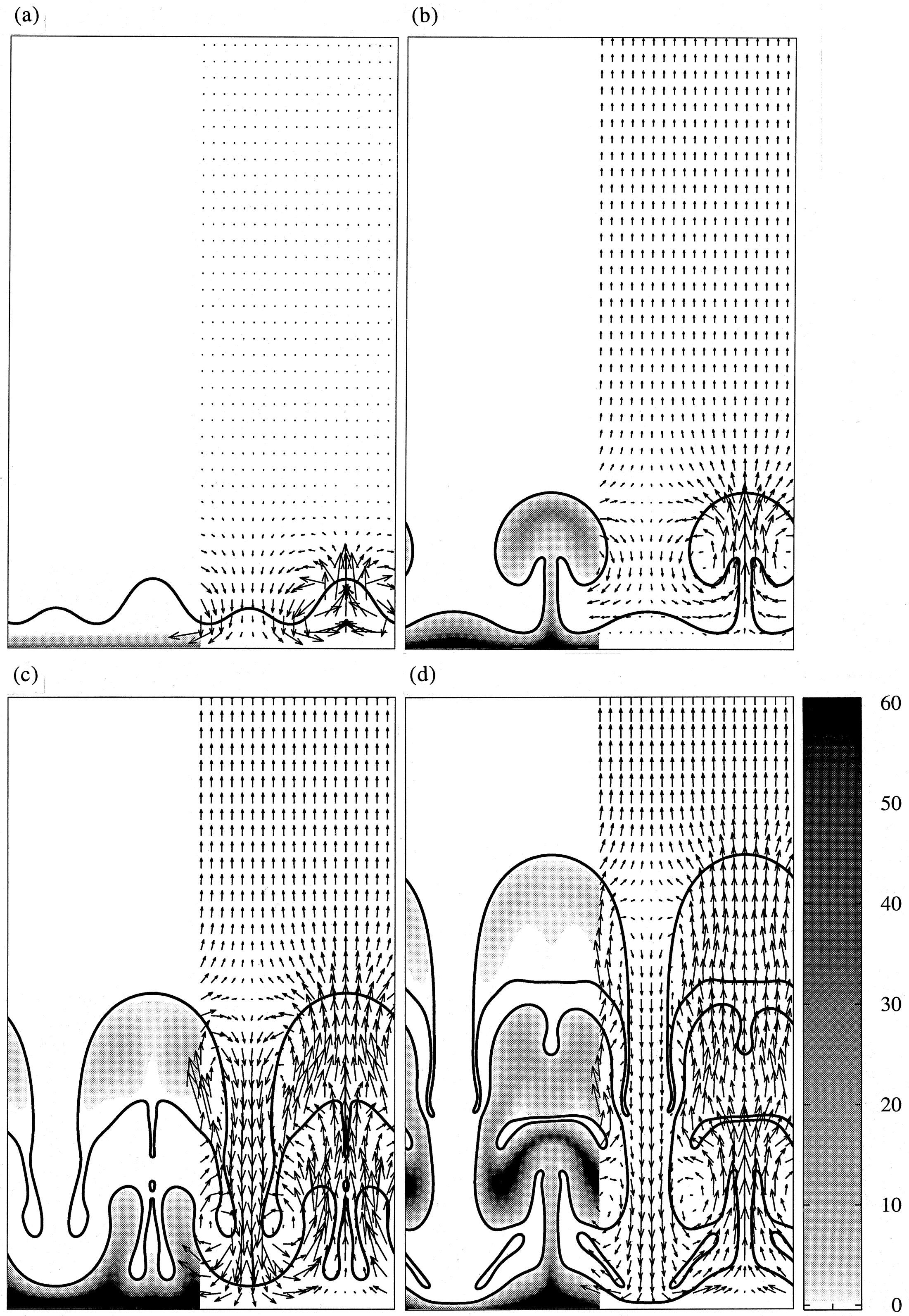

Figure 2. A simulation of film boiling shown at times, t = 2, 14, 30, 40. The interface is plotted as the solid black line, the temperature field is shown on the left and velocity vectors (plotted only at every eighth grid point) are shown on the right. In this sequence, the liquid–vapor interface undergoes a Rayleigh–Taylor instability with subsequent pinch off and rise of a vapor bubble. The upward motion of this bubble causes additional vapor to be pulled away from the wall to form a second bubble directly underneath the first. The calculation is performed in a computational box of dimensions (H_x,H_y) = (57.4, 180), with 150×300 grid resolution and the following dimensionless parameters: $\rho_L/\rho_G=5.22$, $\mu_L/\mu_G=3.37$, $k_L/k_G=3.42$, $c_L/c_G=0.882$, $q_w=10$, Pr = 1.51, $M = 10^{-3}$, σ = 0.024, υ = 0.03. Except for the Morton number, these parameters correspond to those of hydrogen at 8 atm pressure (Maddox, 1983).

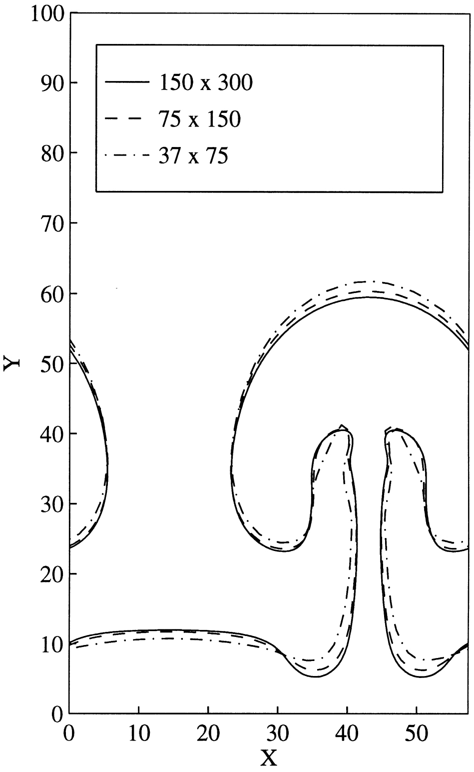

Figure 3. A grid resolution study. The rising vapor bubble is plotted at $t = 18$ for three different grid resolutions for the simulation in figure 2. The interface shapes are very similar even for the coarsest mesh and the 150×300 mesh is an essentially converged solution. These results also include the effect of temporal discretization since the time step decreases with increasing spatial refinement.

flow behind the parent resulting in elongation and entrainment of the son bubble with both bubbles containing similar volumes.

In the simulation the parent bubble assumes a skirted shape. This skirt separates from the parent bubble and is entrained below the son bubble. The detailed structure of the temperature inside the bubbles can be visualized. The parent bubble is released before significant heat can be convected into it. The son bubble, however, is fed by hotter vapor that has just been generated. Heat is convected into its interior as a jet of hot vapor. A liquid drop which had been entrained inside the son bubble during its formation causes the hot vapor to deflect downward.

To illustrate that the results are essentially independent of the mesh, we plot the rising vapor bubble at $t = 18$ for three different grid resolutions. Since we are simulating a highly unsteady problem (unlike the steady rise of a vapor bubble, for example) and the instabilities depend sensitively on the amount of noise present we do not expect identical results. However, in figure 3, the interfaces are obviously very similar even for the coarsest mesh. The 150×300 mesh is an essentially converged solution. These results also include the effect of temporal discretization since the time step decreases with increasing spatial refinement. We also plot the Nusselt number, vapor volume fraction and total interface length vs time for these three resolutions in figure 4. The Nusselt number for the two finer meshes are nearly identical while the vapor volume fraction and total interface length are slightly more sensitive to the resolution. As the interface becomes more convoluted with time, the resolution necessary to resolve the smaller features increases.

For the calculation shown in figure 5 we decrease the Morton number to 10^{-6}. The other parameters are the same except $q_w = 20$, $(H_x, H_y) = \left(\lambda_d^*, 3\lambda_d^*\right)$, $y_c = 24$ and $\epsilon_s = -2.67$. The results are shown at times, $t = 4$, 20, 40, 60. (Again, to better illustrate the temperature field, temperatures above 100 are shown as black. The temperatures for this calculation range from 0 to 510 with

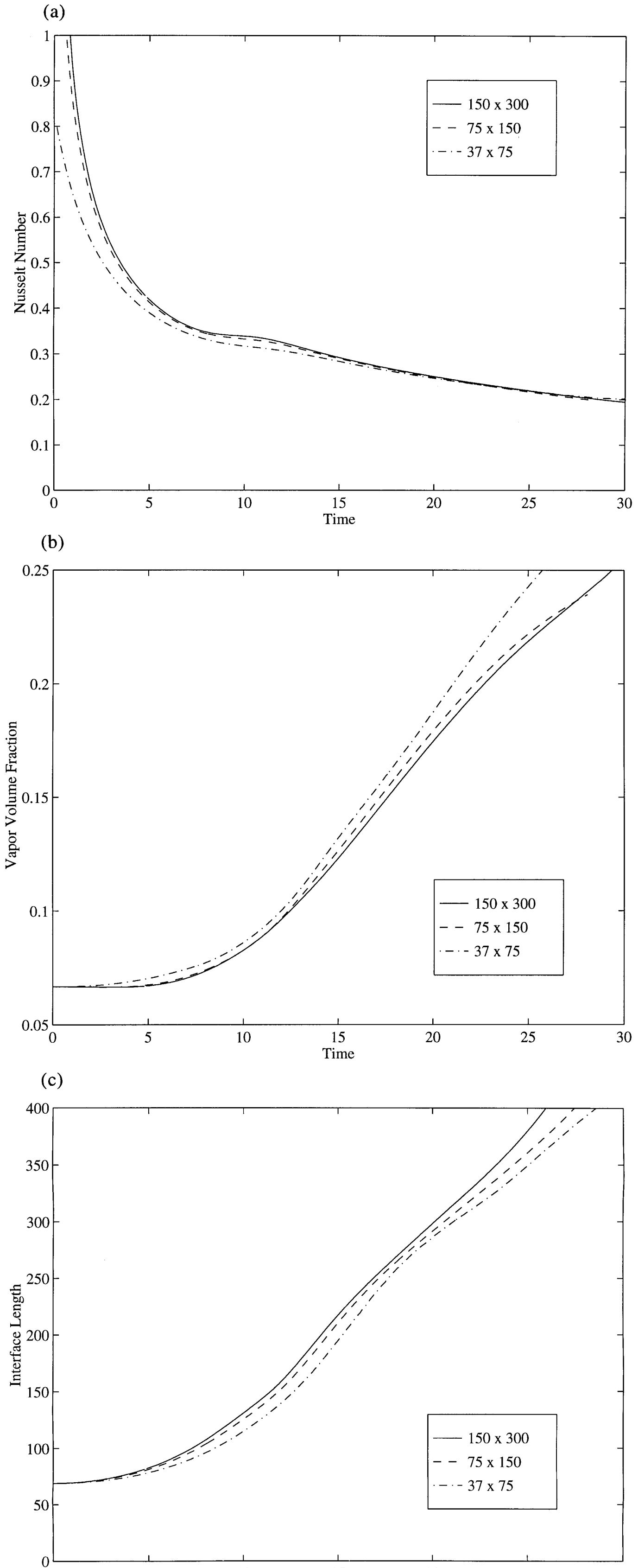

Figure 4. The Nusselt number (a), vapor volume fraction (b) and total interface length (c) are plotted vs time for three different grid resolutions. The Nusselt number for the two finer meshes are nearly identical while the vapor volume fraction and total interface length are slightly more sensitive to the resolution.

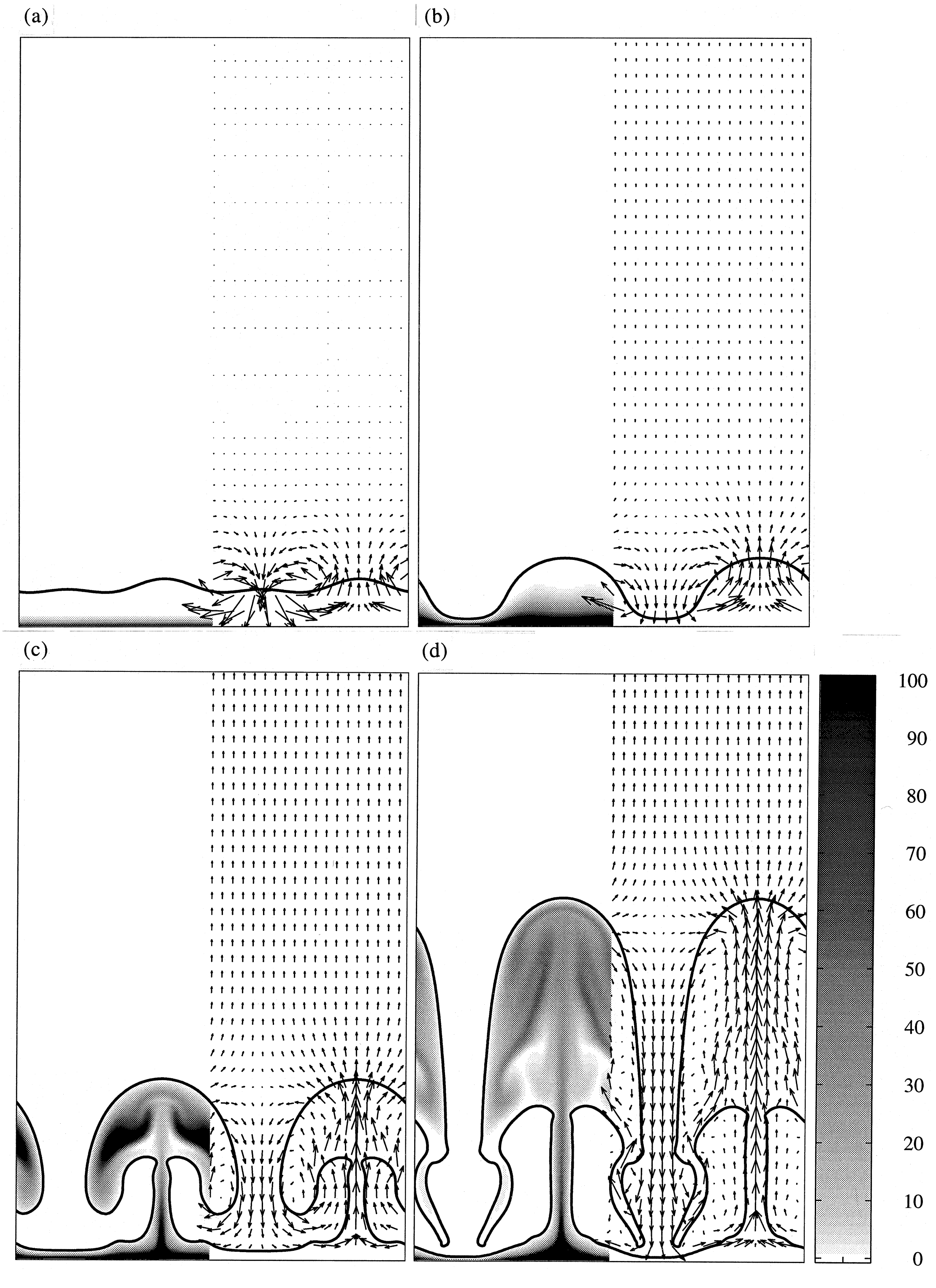

Figure 5. Results from a film boiling simulation at lower Morton number, $M = 10^{-6}$, are shown at times, t = 4, 20, 40, 60. Initially, the interface behaves much like in the previous calculation, figure 2. Here though, the hot vapor is much more quickly convected up into the mushroom shaped bubble, thus preventing the pinch off of its stem. The hot vapor jet impinges on the inside of the bubble cap. Several symmetric, counter-rotating vortices within the bubble act to mix the hot and cold vapor. The parameters are the same as for figure 2 except $q_w = 20$, (H_x, H_y) = (121, 363) $y_c = 24$ and $\epsilon_s = -2.67$.

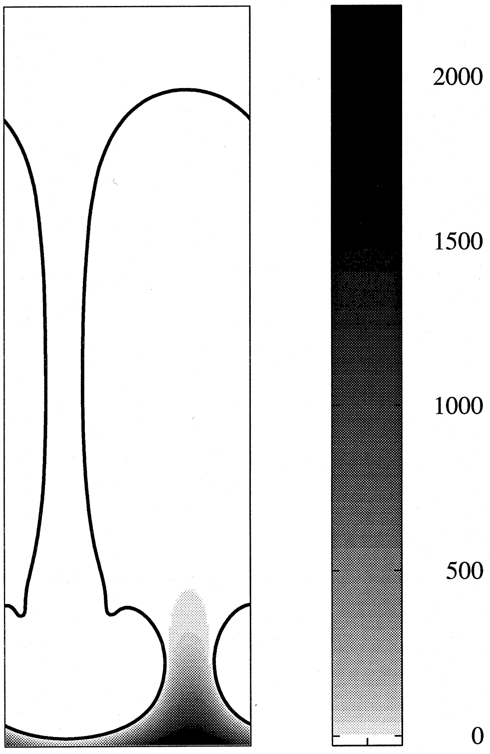

Figure 6. A film boiling calculation at high density ratio, $\rho_L/\rho_G = 1000$. At this high density ratio, the vapor very quickly expands to fill the computational domain as a Taylor bubble. A hot vapor jet is just beginning to emerge into the bubble but most of the interior of the bubble is still relatively cool. $\mu_L/\mu_G = 40$, $k_L/k_G = 10$, $c_L/c_G = 1$, $q_w = 40$, $Pr = 1$, $M = 0.1$, $\sigma = 0$, $\upsilon = 0.008$.

the highest temperatures being at the wall.) Initially, the interface behaves much like in the previous calculation. The Rayleigh–Taylor instability sets in and forms a rising plume of vapor. Here though, the hot vapor is much more quickly convected up into a mushroom shaped bubble, thus preventing the pinch off of its stem. The hot vapor jet impinges on the inside of the bubble cap. Several symmetric, counter-rotating vortices within the bubble act to mix the hot and cold vapor. Hot vapor is carried to lower portions of the bubble and cold vapor is carried up towards the bubble cap. At the high wall temperatures in the simulation shown in figure 5, radiative energy transport from the wall to the liquid–vapor interface can be significant. For example, at $T = 400$ the heat flux due to ideal blackbody radiation can be $q_{\mathrm{rad}} = 2$, 10% of the imposed wall heat flux (Brentari and Smith 1964). The heat flux for real surfaces with non-blackbody emissivity and absorptivity would actually be somewhat lower. However, at this point our code does not include the capability for energy transport by radiation.

Table 2. Values of the exponents and coefficients in equation (49) for four heat transfer correlations

	Exponent			Coefficient		
Correlation	e_1	e_2	e_3	C_1	C_2	C_3
Chang (1959)	0	1	1/3	0.294	1	0.5
Berenson (1961)	1/6	3/2	1/4	0.425	1	0.5
Hamill and Baumeister (1966)	1/6	3/2	1/4	0.41	1	0.95
Klimenko and Shelepen (1982):						
$1/T_w < 1.41 c_G/c_L$	0	1	1/3	0.169	0	1.41
$1/T_w > 1.41 c_G/c_L$	0	1	1/3	0.169	1	0

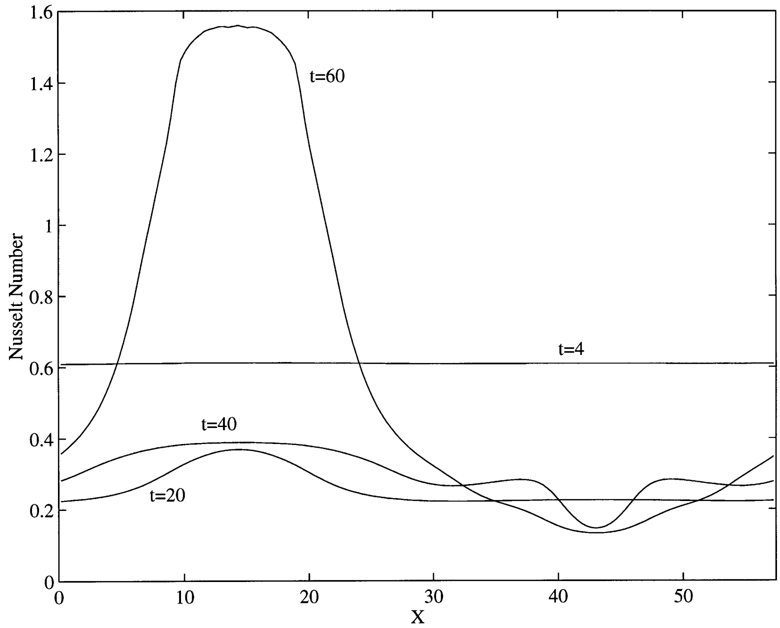

Figure 7. The local Nusselt number from the simulation in figure 5 is plotted at $t = 4, 20, 40, 60$. The heat transfer and thus also the wall temperature vary enormously both in space and time. The highest values occur near the left end of the computational domain where cold liquid is forced near the wall and the vapor layer is thinnest. The lowest heat transfer is at the location directly under the bubble where the vapor layer is thickest.

The numerical calculations in figures 2 and 5 exhibit mushroom shaped bubble growth from the vapor layer. Although mushroom shaped bubbles have been experimentally observed at high heat flux when large amounts of vapor are generated (Ervin *et al.* 1992; Okuyama *et al.* 1988), it is more commonly seen that bubbles pinch off from the vapor layer in a somewhat spheroidal or ellipsoidal shape. In our simulations we cannot expect the bubbles to pinch off as readily. This is simply due to the fact that the computations are done in a two-dimensional geometry and do not provide the necessary radial component of surface force at the bubble stem for realistic pinch off.

For a rough quantitative validation of our numerical predictions we can compare the simulation in figure 2 to experimental data obtained by Class *et al.* (1960) on the film boiling curve (q_w vs T_w) of hydrogen from a flat horizontal surface at 8.7 atm pressure. $q_w = 10$ for figure 2 and the spatially averaged wall temperature (after the initial transient) varies in time from about $T_w = 107$ to 180. The data of Class *et al.* (1960) show that at $q_w = 10$, the wall temperature, T_{w} is about 145 which is within the range of our prediction. For figure 5, $q_w = 20$, however Class *et al.* (1960) did not obtain data at these higher wall heat fluxes and temperatures.

In figure 6 a calculation at a density ratio of $\rho_{\mathrm{L}}/\rho_{\mathrm{G}} = 1000$ is shown at $t = 19$. At this high density ratio, the vapor very quickly expands to fill the computational domain as a Taylor bubble. The interface does not exhibit the convoluted dynamics of the lower density ratio simulations. A hot vapor jet is just beginning to emerge into the bubble, but most of the interior of the bubble is still relatively cool. The computational domain is $(2\lambda_d^*, 6\lambda_d^*)$ with 100×300 grid resolution and the initial interface is described by $y_c = 8$, $\epsilon_s = -1$, $n_s = 2$. The dimensionless parameters used in this calculation are: $\mu_{\mathrm{L}}/\mu_{\mathrm{G}} = 40$, $k_{\mathrm{L}}/k_{\mathrm{G}} = 10$, $c_{\mathrm{L}}/c_{\mathrm{G}} = 1$, $q_w = 40$, $Pr = 1$, $M = 0.1$, $\sigma = 0$, $\upsilon = 0.008$.

An important quantitative characterization of film boiling is the wall heat transfer. Here we briefly review some of the heat transfer correlations developed for laminar film boiling over the last several decades. Chang (1959) was the first to study film boiling on horizontal surfaces. His physical model of film boiling assumed that the average vapor film thickness for a given heat

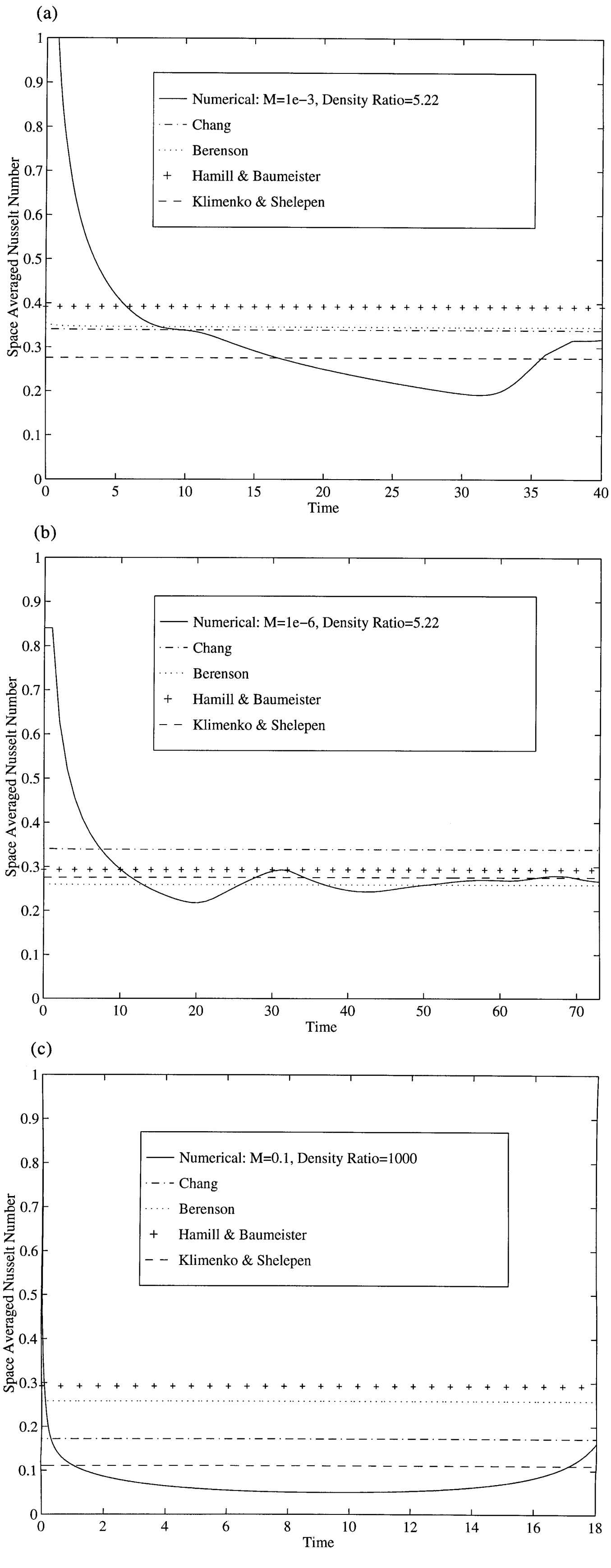

Fig. 8(a–c)—*Caption opposite.*

flux will be equal to a constant critical vapor film thickness for instability of the film. Whereas Chang interpreted the vapor film as having an irregular wavy structure with no apparent length scale, the physical model of film boiling of Berenson (1961) postulated that the vapor generated in the film is released from a regularly spaced array of vapor domes. In his model the most unstable wavelength of the Rayleigh–Taylor instability, λ_d, is the length scale that governs the height, diameter and spacing of the domes. Berenson found that predictions using the correlation developed from this model agreed with his experimental data on n-pentane and carbon tetrachloride to within 10%. Using a similar physical model for the structure of the vapor film, Hamill and Baumeister (1966) derived a correlation based on the hypothesis that the film boiling process operates at a state of maximum entropy generation. Except for two of the coefficients, their correlation turned out to be virtually identical to Berenson's. More recently, Klimenko (1981) and Klimenko and Shelepen (1982) developed a correlation that they found holds within 25% of the experimental measurements by many different researchers on many different fluids, including cryogens. Their correlation uses the same basic physical model as Berenson (1961), but also employs the Reynolds analogy for heat transfer. For laminar flow, the correlations described above can be expressed by

$$N = C_1\left[M^{e_1}Pr\left(1-\frac{\rho_G}{\rho_L}\right)^{e_2}\frac{\rho_G}{\rho_L}\frac{\mu_L}{\mu_G}\frac{k_L}{k_G}\left(\frac{C_2}{T_w}+C_3\frac{c_G}{c_L}\right)\right]^{e_3}, \qquad [49]$$

where the particular values of the exponents, e_1, e_2, e_3, and coefficients, C_1, C_2, C_3, for each of the four correlations are given in table 2.

In figure 7 we plot the local values of the Nusselt number from the simulation in figure 5 at $M = 10^{-6}$ vs x for several different times. Obviously, the heat transfer and thus also the wall temperature vary enormously both in space and time. In general, the highest values occur near the left end of the computational domain where cold liquid is forced near the wall and the vapor layer is thinnest. The lowest heat transfer is at the location directly under the bubble where the vapor layer is thickest. The heat transfer behavior for the simulation in figure 2 at $M = 10^{-3}$ is similar. The physical models of film boiling used to develop the above correlations neglect these spatial and temporal variations in wall temperature and vapor film thickness. However, it is clear that these variations are directly associated with the local, instantaneous heat transfer. Thus the detailed small-scale information about the interface behavior, thermal and flow fields provided by these simulations can, it is hoped, identify crucial features, parameters and assumptions for improved physical models and correlations.

In order to compare the simulations with the heat transfer predicted from [49], we spatially average the wall heat transfer values from our simulations and plot this average vs time in figure 8. The comparison is shown for the simulations in: (a) figure 2 with $M = 10^{-3}$, $\rho_L/\rho_G = 5.22$; (b) figure 5 with $M = 10^{-6}$, $\rho_L/\rho_G = 5.22$; and (c) figure 6 with $M = 10^{-1}$, $\rho_L/\rho_G = 1000$. After an initial transient the numerical results for Nusselt number agree rather well with the correlations and certainly to within the accuracy of the 25% experimental data scatter reported by Klimenko and Shelepen (1982). The numerical results for lower Morton number in figure 8(b) settle down to what may be a steady value at longer times and at these later times are in especially good agreement with the correlation of Klimenko and Shelepen (1982), Berenson (1961), Hamill and Baumeister (1966). For the high density ratio calculation in (c) the Nusselt number is still evolving in time and it is difficult to make a comparison with the correlations.

Figure 8. Predicted average Nusselt number compared with [49] for the correlations of Chang (1959), Berenson (1961), Hamill and Baumeister (1966) and Klimenko and Shelepen (1982), for the simulations in (a) figure 2 with $M = 10^{-3}$, $\rho_L/\rho_G = 5.22$, (b) figure 5 with $M = 10^{-6}$, $\rho_L/\rho_G = 5.22$ and (c) figure 6 with $M = 10^{-1}$, $\rho_L/\rho_G = 1000$. After an initial transient the numerical results for Nusselt number agree well with the correlations and certainly to within the accuracy of the 25% experimental data scatter reported by Klimenko and Shelepen (1982). For the high density ratio calculation in (c) the Nusselt number is still evolving in time and it is difficult to make a comparison to the correlations.

Although the agreement is relatively good, conclusions that can be drawn from these plots must be tempered by the fact that the numerical results are only in two-dimensions and do not simulate a complete bubble ebullition cycle.

5. CONCLUSIONS

A numerical method for direct numerical simulation of film boiling has been presented. The method is based on the finite difference/front tracking method of Unverdi and Tryggvason (1992), but the addition of phase change has required extensive reformulation. To demonstrate the ability of the method to deal with a complex interface geometry we have presented several two-dimensional simulations of film boiling, following the growth of the initial instability of the film, through the departure of a vapor bubble. The overall heat transfer rates and wall temperatures are in reasonably good agreement with experimental observations and correlations, but there are differences between the computed interface geometry and what is seen in experiments. The computed bubbles do not readily pinch off from the vapor layer and this is due to the fact that the computations are only two-dimensional. The formulation, however, applies equally well to axisymmetric and fully three-dimensional flows. The key difficulties with the three-dimensional extension are related to the treatment of the front and most of those have already been dealt with in the original, isothermal version of the method. With some minor modifications to accommodate for the contact of the phase interface with rigid walls, we also plan to extend the capability of the method to be able to investigate the nucleate and transition boiling regimes.

Acknowledgements—This work was supported by NASA Graduate Student Fellowship NGT-51070 and NSF Grant CTS-9503208. Some of the computations were done at the Center for Parallel Computing (CPC) at the University of Michigan. We would also like to acknowledge helpful discussions with J.U. Brackbill of the Los Alamos National Laboratory.

REFERENCES

Alexiades, V. and Solomon, A. D. (1993) *Mathematical Modeling of Melting and Freezing Processes*. Hemisphere, Washington, DC.

Ammerman, C. N., You, S. M. and Hong, Y. S. (1996) Identification of pool boiling heat transfer mechanisms from a wire immersed in saturated FC-72 using a single-photo/LDA method. *J. Heat Transfer* **118,** 117–123.

Berenson, P. J. (1961) Film boiling heat transfer from a horizontal surface. *J. Heat Transfer* **83C** (3), 351–358.

Bornhorst, W. J. and Hatsopoulos, G. N. (1967a) Analysis of a liquid vapor phase change by the methods of irreversible thermodynamics. *J. Appl. Mech.* **34,** 840–846.

Bornhorst, W. J. and Hatsopoulos, G. N. (1967b) Bubble-growth calculations without neglect of interfacial discontinuities. *J. Appl. Mech.* **34,** 847–853.

Brentari, E. G. and Smith, R. V. (1964) Nucleate and film pool boiling design correlations for O_2, N_2, H_2 and He. *Int. Adv. Cryogenic Engng.* **10,** 325–341.

Chang, Y. P. (1959) Wave theory of heat transfer in film boiling. *J. Heat Transfer* **81C,** 1–12.

Chorin, A. J. (1968) Numerical solution of the Navier–Stokes equations. *Math. Comput.* **22,** 745–762.

Class, C. R., DeHaan, J. R., Piccone, M. and Cost, R. B. (1960) Boiling heat transfer to liquid hydrogen from flat surfaces. *Adv. Cryogenic. Engng.* **5,** 254–261.

Dalle Donne, M. and Ferranti, M. P. (1975) The growth of vapor bubbles in superheated sodium. *Int. J. Heat Mass Transfer* **18,** 477–493.

Delhaye, J. M. (1974) Jump conditions and entropy sources in two-phase systems, local instant formulation. *Int. J. Multiphase Flow* **1,** 395–409.

Ervin, J. S., Merte, H. Jr., Keller, R. B. and Kirk, K. (1992) Transient pool boiling in microgravity. *Int. J. Heat Mass Transfer* **35,** 659–674.

Esmaeeli, A. and Tryggvason, G. (1996) An inverse energy cascade in 2-dimensional low Reynolds number bubbly flows. *J. Fluid Mech.* **314,** 315–330.

Hamill, T. D. and Baumeister, K. J. (1966) Film boiling heat transfer from a horizontal surface as an optimal boundary value process. *Proc. 3rd Int. Heat Trans. Conf.* **4,** 59–64.

Harlow, F. H. and Welch, J. E. (1965) Numerical calculation of time-dependent viscous incompressible flow of fluid with free surface. *Phys. Fluids* **8,** 2182–2189.

Huang, A. and Joseph, D. D. (1992) Instability of the equilibrium of a liquid below its vapour between horizontal heated plates. *J. Fluid Mech.* **242,** 235–247.

Huang, A. and Joseph, D. D. (1993) Stability of liquid–vapor flow down an inclined channel with phase change. *Int. J. Heat Mass Transfer* **36,** 663–672.

Ishii, M. (1975) *Thermo-fluid Dynamic Theory of Two-Phase Flow*. Eyrolles, Paris.

Juric, D. and Tryggvason, G. (1996) A front-tracking method for dendritic solidification. *J. Comp. Phys.* **123,** 127–148.

Klimenko, V. V. (1981) Film boiling on a horizontal plate—new correlation. *Int. J. Heat Mass Transfer* **24,** 69–79.

Klimenko, V. V. and Shelepen, A. G. (1982) Film boiling on a horizontal plate—a supplementary communication. *Int. J. Heat Mass Transfer* **25,** 1611–1613.

Lee, H. S. (1993) Vapor bubble dynamics in microgravity, Ph.D. Dissertation, The University of Michigan.

Lee, R. C. and Nydahl, J. E. (1989) Numerical calculation of bubble growth in nucleate boiling from inception through departure. *J. Heat Transfer* **111,** 474–479.

Lienhard, J. H. (1994) Snares of pool boiling research: putting our history to use. In *Proceedings of the Tenth International Heat Transfer Conference*, ed. G. F. Hewitt, Vol. 1, pp. 333–348.

Maddox, R. N. (1983) Properties of saturated fluids. In *Heat Exchanger Design Handbook*. Hemisphere, New York.

Mikic, B. B., Rohsenow, W. M. and Griffith, P. (1970) On bubble growth rates. *Int. J. Heat Mass Transfer* **13,** 657–666.

Nas, S. and Tryggvason, G. (1993) Computational investigation of thermal migration of bubbles and drops. In *Fluid Mechanics Phenomena in Microgravity*, AMD 174/FED 175, pp. 71–83. ASME, New York.

Nobari, M. R., Jan, Y.-J. and Tryggvason, G. (1996) Head on collision of drops—a numerical investigation. *Phys. Fluids* **8,** 29–42.

Okuyama, K., Kozawa, Y., Inoue, A. and Aoki, S. (1988) Transient boiling heat transfer characteristics of R113 at large stepwise power generation. *Int. J. Heat Mass Transfer* **31,** 2161–2174.

Patil, R. K. and Prusa, J. (1991) Numerical solutions for asymptotic, diffusion controlled growth of a hemispherical bubble on an isothermally heated surface: In *Experimental/Numerical Heat Transfer in Combustion and Phase Change*, HTD 170, pp. 63–70. ASME, New York.

Peskin, C. S. (1977) Numerical analysis of blood flow in the heart. *J. Comput. Phys.* **25,** 220–252.

Peskin, C. S. and McQueen, D. M. (1994) A general method for the computer simulation of biological systems interacting with fluids. In *SEB Symposium on Biological Fluid Dynamics*. Leeds, England.

Plesset, M. S. and Zwick, S. A. (1954) The growth of vapor bubbles in superheated liquids. *J. Appl. Phys.* **25,** 493–500.

Prosperetti, A. and Plesset, M. S. (1978) Vapor bubble growth in a superheated liquid. *J. Fluid Mech.* **85,** 349–368.

Qian, J., Tryggvason, G. and Law, C. K. (1997) A front tracking method for the motion of premixed flames. *J. Comp. Phys.* **0,** Submitted.

Rayleigh, Lord (1917) On the pressure developed in a liquid during the collapse of a spherical cavity. *Phil. Mag.* **34,** 94–98.

Schrage, R. W. (1953) *A Theoretical Study of Interphase Mass Transfer*. Columbia University Press, New York.

Shoji, M., Witte, L. C. and Sankaran, S. (1990) The influence of surface conditions and subcooling on film-transition boiling. *Exptl. Thermal Fluid Sci.* **3,** 280–290.

Son, G. and Dhir, V. K. (1995) Two-dimensional numerical simulation of saturated film boiling on a horizontal surface. In *Proc. ASME/JSME Thermal Engineering Joint Conf.*, eds L. S. Fletcher and T. Aihara, pp. 257–264. ASME, New York.

Tanasawa, I. (1991) Advances in condensation heat transfer. In *Advances in Heat Transfer*, eds J. P. Hartnett and T. F. Irvine, Jr., pp. 55–139. Academic Press, New York.

Tarshis, L. A. and Tiller, W. A. (1966) In *Crystal Growth*, ed. H. S. Peiser, pp. 709–719. Pergamon, London.

Truskinovsky, L. (1993) Kinks versus shocks. In *Shock Induced Transitions and Phase Structures in General Media*, eds J. E. Dunn *et al.*, pp. 185–229. Springer-Verlag, Berlin.

Unverdi, S. O. and Tryggvason, G. (1992) A front-tracking method for viscous, incompressible, multi-fluid flows. *J. Comp. Phys.* **100,** 25–37.

Welch, S. W. J. (1995) Local simulation of two-phase flows including interface tracking with mass transfer. *J. Comp. Phys.* **121,** 142–154.